Geophys. J. Int. (2011) **186,** 1245–1254 doi: 10.1111/j.1365-246X.2011.05101.x

Anisotropic poroelasticity and wave-induced fluid flow: harmonic finite-element simulations

J. M. Carcione,[1] J. E. Santos[2] and S. Picotti[1]

[1] *Istituto Nazionale di Oceanografia e di Geofisica Sperimentale (OGS), Borgo Grotta Gigante* 42c, 34010 *Sgonico, Trieste, Italy. E-mail: jcarcione@inogs.it*
[2] *CONICET, Departamento de Geofísica Aplicada, Fac. Ciencias Astronómicas y Geofísicas, UNLP, Paseo del Bosque S/N, La Plata, 1900, Argentina, and Purdue University, West Lafayette,* IN 47907, *USA*

Accepted 2011 June 4. Received 2011 May 19; in original form 2011 March 6

SUMMARY

A dominant *P*-wave attenuation mechanism in reservoir rocks at seismic frequencies is due to wave-induced fluid flow (mesoscopic loss). The *P*-wave induces a fluid-pressure difference at mesoscopic-scale inhomogeneities (larger than the pore size but smaller than the wavelength), generating fluid flow and slow (diffusion) Biot waves. The theory has been developed in the 1970s for the symmetry axis of the equivalent transversely isotropic (TI) medium corresponding to a finely layered medium, and has recently been generalized to all propagation angles. The new theory states that the fluid-flow direction is perpendicular to the layering plane and it is independent of the loading direction. As a consequence, the relaxation behaviour can be described by a single relaxation function, since the medium consists of plane homogeneous layers. Besides *P*-wave losses, the coupling between the *qP* and *qSV* waves generates shear-wave anisotropic velocity dispersion and attenuation.

In this work, we introduce a set of quasi-static numerical experiments to determine the equivalent viscoelastic TI medium to a finely layered poroelastic medium, which is validated using a recently developed analytical solution. The modelling technique is the finite-element (FE) method, where the equations of motion are solved in the space-frequency domain. Numerical rock physics may, in many circumstances, offer an alternative to laboratory measurements. Numerical experiments are inexpensive and informative since the physical process of wave propagation can be inspected during the experiment. Moreover, they are repeatable, essentially free from experimental errors, and may easily be run using alternative models of the rock and fluid properties.

We apply the methodology to the Utsira aquifer of the North Sea, where carbon dioxide (CO_2) has been injected during the last 15 years. The tests consider alternating layers of the same rock saturated with gas and brine and a sequence of gas-saturated sandstone and mudstone layers, which represent possible models of the reservoir and cap rock of the aquifer system. The numerical examples confirm the new theory and illustrate the implementation of the harmonic tests to determine the complex and frequency-dependent effective stiffnesses and the associated wave velocities and quality factors.

Key words: Elasticity and anelasticity; Seismic anisotropy; Seismic attenuation; Wave propagation.

1 INTRODUCTION

It is known that one of the major causes of seismic attenuation in porous media is wave-induced fluid flow (Pride *et al.* 2004), which occurs at mesoscopic scales. The *P*-wave induces a fluid-pressure difference at mesoscopic-scale inhomogeneities (larger than the pore size but smaller than the wavelength, typically tens of centimetres), generating fluid flow and slow (diffusion) Biot waves (continuity of pore pressure is achieved by energy conversion to slow *P* waves which diffuse away from the interfaces). White *et al.* (1975) were the first to introduce the mesoscopic-loss mechanism based on approximations in the framework of Biot theory (White model). They considered porous and thin plane layers. This has been the first so-called 'mesoscopic-loss' mechanism. The mesoscopic-loss theory has been further refined by other researchers. A review can be found in Carcione & Picotti (2006), Carcione (2007), Carcione *et al.* (2010) and Müller *et al.* (2010).

Attenuation in rocks may occur at other spatial scales: macroscopic and microscopic. The attenuation mechanism predicted by Biot theory (Biot 1962; Carcione 2007) has a macroscopic nature. It is the wavelength-scale equilibration between the peaks and troughs of the fast *P* wave. The related relaxation peak is mainly

located at the kHz's range and moves towards the high frequencies with increasing viscosity and decreasing permeability, which is the opposite behaviour of the mesoscopic peak. On the other hand, microscopic models, such as the 'squirt-flow' and 'grain friction' models seem to be important at high (laboratory-scale) frequencies (Pride *et al.* 2004).

The two aspects of the theory are thin layering and wave-induced interlayer fluid flow. A finely layered medium behaves as a TI equivalent medium at long wavelengths. Bruggeman (1937) and later other investigators studied the problem using different approaches, for example, Riznichenko (1949), Postma (1955), Backus (1962) and Carcione (1992), who generalized the theory to the anelastic case to model Q-(quality factor) anisotropy. They have considered single-phase (non-porous) media. On the other hand, White *et al.* (1975) obtained the complex and frequency-dependent P-wave stiffness associated with the symmetry axis of thin poroelastic layers. The next step has been achieved by Gelinsky & Shapiro (1997) who obtained the relaxed and unrelaxed stiffnesses of the equivalent poro-viscoelastic medium. Krzikalla & Müller (2011) combined the two previous models to obtain the five complex and frequency-dependent stiffnesses of the equivalent medium. They consider a 1-D character of the fluid pressure equilibration process between the poroelastic layers, assuming that the fluid-flow direction is perpendicular to the layering plane. As a consequence, the model considers one relaxation function, corresponding to the symmetry-axis P-wave stiffness. Therefore, knowing this relaxation function and the high- and low-frequency elastic limits of the stiffness tensor, Krzikalla & Müller (2011) obtained the five complex and frequency-dependent stiffnesses of the equivalent viscoelastic medium. We refer to this new theory as Backus/White model. Moreover, Krzikalla & Müller (2011) carried out time-domain FE simulations of poroelastic relaxation analogous to those described in Wenzlau *et al.* (2010), using a commercial simulation package.

To test the model and provide a more general modelling tool, we perform numerical simulations using an upscaling procedure to obtain the complex stiffnesses of the effective TI medium. It consists in the simulation of oscillatory compressibility and shear tests in the space-frequency domain, which enable us to obtain the complex stiffnesses. The method is illustrated in Picotti *et al.* (2010) and Santos *et al.* (2011) for single-phase media and it is generalized here for porous media. We use the FE method in the frequency domain to compute the solutions of the associated boundary value problem. We obtain the quality factors and velocities as a function of frequency and propagation angle from the complex stiffnesses and composite density.

The methodology is applied to the problem of CO_2 detection and monitoring. Specifically, CO_2 has been injected into the Utsira formation at the Sleipner field in the North Sea since 1996. To follow the migration of the CO_2, seismic monitoring surveys have been carried periodically. Therefore, to quantify the amount of gas saturation it is essential to fully characterize the properties of the Utsira formation, in the reservoir and in the cap rock, where possible leakages may occur. We consider two possible scenarios present *in situ*: alternating layers of gas and brine in the same rock frame (the Utsira sand) and a sequence of thin layers of gas- and water-saturated Utsira sandstone and low-permeability mudstone.

2 THE STRESS–STRAIN RELATIONS

Let us consider isotropic poroelastic layers and denote the time variable by t, the frequency by f and the position vector by $\mathbf{x} = (x, y, z) = (x_1, x_2, x_3)$. Let $u^s(\mathbf{x}) = (u_1^s, u_2^s, u_3^s)$ and $u^f(\mathbf{x}) = (u_1^f, u_2^f, u_3^f)$ indicate the time Fourier transform of the displacement vector of the solid and fluid (relative to the solid) phases, respectively (if U^f is the fluid displacement vector, $u^f = \phi(U^f - u^s)$, where ϕ is the porosity). Also, set $u = (u^s, u^f)$, let $\sigma_{ij}(u)$ and $p_f(u)$ denote the time Fourier transform of the total stress and the fluid pressure, respectively, and let $\epsilon_{ij}(u^s)$ be the strain tensor of the solid phase. The frequency-domain stress–strain relations of a single plane layer n in a sequence of N layers, are (Carcione 2007)

$$\sigma_{kl}(u) = 2\mu^{(n)}\,\varepsilon_{kl}(u^s) + \delta_{kl}\left(\lambda_G^{(n)}\,\nabla\cdot u^s + \alpha^{(n)}M^{(n)}\nabla\cdot u^f\right), \tag{1}$$

$$p_f(u) = -\alpha^{(n)}M^{(n)}\nabla\cdot u^s - M^{(n)}\nabla\cdot u^f. \tag{2}$$

For each layer n, the coefficient μ is the shear modulus of the bulk material, considered to be equal to the shear modulus of the dry matrix. Also

$$\lambda_G = K_G - \frac{2}{3}\mu, \tag{3}$$

with K_G the bulk modulus of the saturated material (Gassmann modulus). The coefficients in eqs (1) and (2) can be obtained from the relations (Carcione 2007)

$$\alpha = 1 - \frac{K_m}{K_s}, \quad M = \left(\frac{\alpha-\phi}{K_s} + \frac{\phi}{K_f}\right)^{-1},$$
$$K_G = K_m + \alpha^2 M, \tag{4}$$

where K_s, K_m and K_f denote the bulk moduli of the solid grains, dry matrix and saturant fluid, respectively. The coefficient α is known as the effective stress coefficient of the bulk material. Let ρ_s and ρ_f denote the mass densities of the solid grains and fluid, respectively, and let

$$\rho = (1-\phi)\rho_s + \phi\rho_f \tag{5}$$

denote the mass density of the bulk material. We define the matrices

$$\mathcal{P} = \begin{pmatrix} \rho I & \rho_f I \\ \rho_f I & mI \end{pmatrix} \quad \text{and} \quad \mathcal{B} = \begin{pmatrix} 0I & 0I \\ 0I & bI \end{pmatrix}. \tag{6}$$

which are positive definite and non-negative, respectively. Here, I is the 3×3 identity matrix, the mass coupling coefficient m represents the inertial effects associated with dynamic interactions between the solid and fluid phases, while the coefficient b includes theviscous coupling effects between such phases. They are given by the relations

$$b = \frac{\eta}{\kappa}, \qquad m = \frac{\mathcal{T}\rho_f}{\phi}, \tag{7}$$

where η is the fluid viscosity, κ is the frame permeability and $\mathcal{T}$ is known as the structure or tortuosity factor. Next, let $\mathcal{L}(u)$ be the second-order differential operator defined by

$$\mathcal{L}(u) = [\nabla\cdot\sigma(u), -\nabla p_f(u)]^\top. \tag{8}$$

Then, if $\omega = 2\pi\ f$ is the angular frequency, Biot's equations of motion, stated in the space-frequency domain, are

$$-\omega^2\mathcal{P}u(x,\omega) + \mathrm{i}\omega\mathcal{B}u(x,\omega) - \mathcal{L}[u(x,\omega)] = 0, \tag{9}$$

which are complemented with eqs (1) and (2). We have ignored external sources in eq. (9). Over the seismic band of frequencies, the inertial (acceleration) term $(-\omega^2 Pu(x,\omega))$ is always negligible relative to the viscous resistance and can be discarded. Therefore, at this frequency band, the effects of wave-induced fluid flow are described by the quasistatic Biot theory, i.e. stress equilibrium within

the porous matrix and Darcy's flow of pore fluid. Then, the system equation to solve is the diffusion equation:

$$i\omega B u(x,\omega) - L[u(x,\omega)] = 0. \tag{10}$$

Let us consider x_1 and x_3 as the horizontal and vertical coordinates, respectively. As shown by Gelinsky & Shapiro (1997), the medium behaves as a TI medium with a vertical symmetry axis (the x_3-axis) at long wavelengths. They obtained the relaxed and unrelaxed limits, that is, the low- and high-frequency limit real-valued stiffnesses, respectively. At all frequencies, the medium behaves as an equivalent (or effective) TI viscoelastic medium with complex and frequency-dependent stiffnesses, p_{IJ}, $I, J = 1, \ldots, 6$. A model has been proposed by Krzikalla & Müller (2011) and is given in detail in Appendix A.

Denoting by τ_{ij} the stress tensor of the equivalent TI medium, the corresponding stress-strain relations, stated in the space-frequency domain, are (Carcione 1992; Carcione 2007)

$$\tau_{11}(u) = p_{11}\,\epsilon_{11}(u^s) + p_{12}\,\epsilon_{22}(u^s) + p_{13}\,\epsilon_{33}(u^s), \tag{11}$$

$$\tau_{22}(u) = p_{12}\,\epsilon_{11}(u^s) + p_{11}\,\epsilon_{22}(u^s) + p_{13}\,\epsilon_{33}(u^s), \tag{12}$$

$$\tau_{33}(u) = p_{13}\,\epsilon_{11}(u^s) + p_{13}\,\epsilon_{22}(u^s) + p_{33}\,\epsilon_{33}(u^s), \tag{13}$$

$$\tau_{23}(u) = 2\,p_{55}\,\epsilon_{23}(u^s), \tag{14}$$

$$\tau_{13}(u) = 2\,p_{55}\,\epsilon_{13}(u^s), \tag{15}$$

$$\tau_{12}(u) = 2\,p_{66}\,\epsilon_{12}(u^s), \tag{16}$$

where we have assumed a closed system. This can be done for the undrained composite medium, for which the variation of fluid content $\zeta = -\mathrm{div}\ u^f$ is equal to zero. This approach provides the complex velocities of the fast modes. To obtain also the complex velocity of the slow Biot wave, one needs to consider the stiffness coefficients related to the variation fluid content and fluid pressure, where the stiffness matrix has a 7×7 dimension (Carcione 2007). This calculation requires to know the complex and frequency-dependent version of the coefficients B_6^*, B_7^* and B_8^* (Appendix A). The p_{IJ} are the complex and frequency-dependent Voigt stiffnesses predicted by Krzikalla & Müller (2011) to be determined with the harmonic experiments. In the next section we present a numerical procedure to determine the coefficients in eqs (11)–(16) and the corresponding phase velocities and quality factors. These properties, which depend on frequency and propagation direction, are given in Appendix B. We show that for this purpose it is sufficient to perform a collection of oscillatory tests on representative 2-D samples of the viscoelastic material.

3 DETERMINATION OF THE STIFFNESSES

In order to determine the coefficients in eqs (11)–(16) we proceed as follows. We solve eq. (9) in the 2-D case on a reference square $\Omega = (0, L)^2$ with boundary Γ in the (x_1, x_3)-plane. Set $\Gamma = \Gamma^L \cup \Gamma^B \cup \Gamma^R \cup \Gamma^T$, where

$$\Gamma^L = \{(x_1, x_3) \in \Gamma : x_1 = 0\}, \quad \Gamma^R = \{(x_1, x_3) \in \Gamma : x_1 = L\},$$

$$\Gamma^B = \{(x_1, x_3) \in \Gamma : x_3 = 0\}, \quad \Gamma^T = \{(x_1, x_3) \in \Gamma : x_3 = L\}.$$

Denote by ν the unit outer normal on Γ and let χ be a unit tangent on Γ so that $\{\nu, \chi\}$ is an orthonormal system on Γ. The sample is subjected to time-harmonic compressions $\Delta P \exp(\mathrm{i}\omega t)$, where P denotes pressure, and time-harmonic tangential forces $\Delta G \exp(\mathrm{i}\omega t)$, where G is the shear stress (Fig. 1).

It follows how to obtain the stiffness components.

(i) p_{33}: We solve eq. (9) in Ω with the following boundary conditions

$$\sigma(u)\nu \cdot \nu = -\Delta P, \quad (x_1, x_3) \in \Gamma^T, \tag{17}$$

$$\sigma(u)\nu \cdot \chi = 0, \quad (x_1, x_3) \in \Gamma^T, \tag{18}$$

$$\sigma(u)\nu \cdot \chi = 0, \quad (x_1, x_3) \in \Gamma^L \cup \Gamma^R, \tag{19}$$

$$u^s \cdot \nu = 0, \quad (x_1, x_3) \in \Gamma^L \cup \Gamma^R, \tag{20}$$

$$u^s = 0, \quad (x_1, x_3) \in \Gamma^B, \tag{21}$$

$$u^f \cdot \nu = 0, \quad (x_1, x_3) \in \Gamma. \tag{22}$$

In this experiment $\epsilon_{11}(u^s) = \epsilon_{22}(u^s) = \zeta = 0$ and from eq. (9) we see that this experiment determines p_{33} as follows.

Denoting by V the original volume of the sample, its (complex) oscillatory volume change, $\Delta V(\omega)$, we note that

$$\frac{\Delta V(\omega)}{V} = -\frac{\Delta P}{p_{33}(\omega)}, \tag{23}$$

valid in the quasi-static case. Eq. (23) is another form of the stress-strain relation, where $\Delta V/V$ is the strain and $-\Delta P$ is the stress. After solving eq. (9) with the boundary conditions (17)–(22), the vertical displacements ${u^s}_3(x, L, \omega)$ on Γ^T allow us to obtain an average vertical displacement $u_3^{s,T}(\omega)$ at the boundary Γ^T. Then, for each frequency ω, the volume change produced by the compressibility test can be approximated by $\Delta V(\omega) \approx L u_3^{s,T}(\omega)$, which enable us to compute $p_{33}(\omega)$ by using the relation (23).

(ii) p_{11}: The boundary conditions are

$$\sigma(u)\nu \cdot \nu = -\Delta P, \quad (x_1, x_3) \in \Gamma^R, \tag{24}$$

$$\sigma(u)\nu \cdot \chi = 0, \quad (x_1, x_3) \in \Gamma^R, \tag{25}$$

$$\sigma(u)\nu \cdot \chi = 0, \quad (x_1, x_3) \in \Gamma^B \cup \Gamma^T, \tag{26}$$

$$u^s \cdot \nu = 0, \quad (x_1, x_3) \in \Gamma^B \cup \Gamma^T, \tag{27}$$

$$u^s = 0, \quad (x_1, x_3) \in \Gamma^L, \tag{28}$$

$$u^f \cdot \nu = 0, \quad (x_1, x_3) \in \Gamma. \tag{29}$$

In this experiment $\epsilon_{33}(u^s) = \epsilon_{22}(u^s) = \zeta = 0$ and from eq. (11) we have that this experiment determines p_{11} in the same way indicated for p_{33}.

(iii) p_{55}: The boundary conditions are

$$-\sigma(u)\nu = g, \quad (x_1, x_3) \in \Gamma^T \cup \Gamma^L \cup \Gamma^R, \tag{30}$$

$$u^s = 0, \quad (x_1, x_3) \in \Gamma^B, \tag{31}$$

$$u^f \cdot \nu = 0, \quad (x_1, x_3) \in \Gamma, \tag{32}$$

where

$$g = \begin{cases} (0, \Delta G), & (x_1, x_3) \in \Gamma^L, \\ (0, -\Delta G), & (x_1, x_3) \in \Gamma^R, \\ (-\Delta G, 0), & (x_1, x_3) \in \Gamma^T. \end{cases}$$

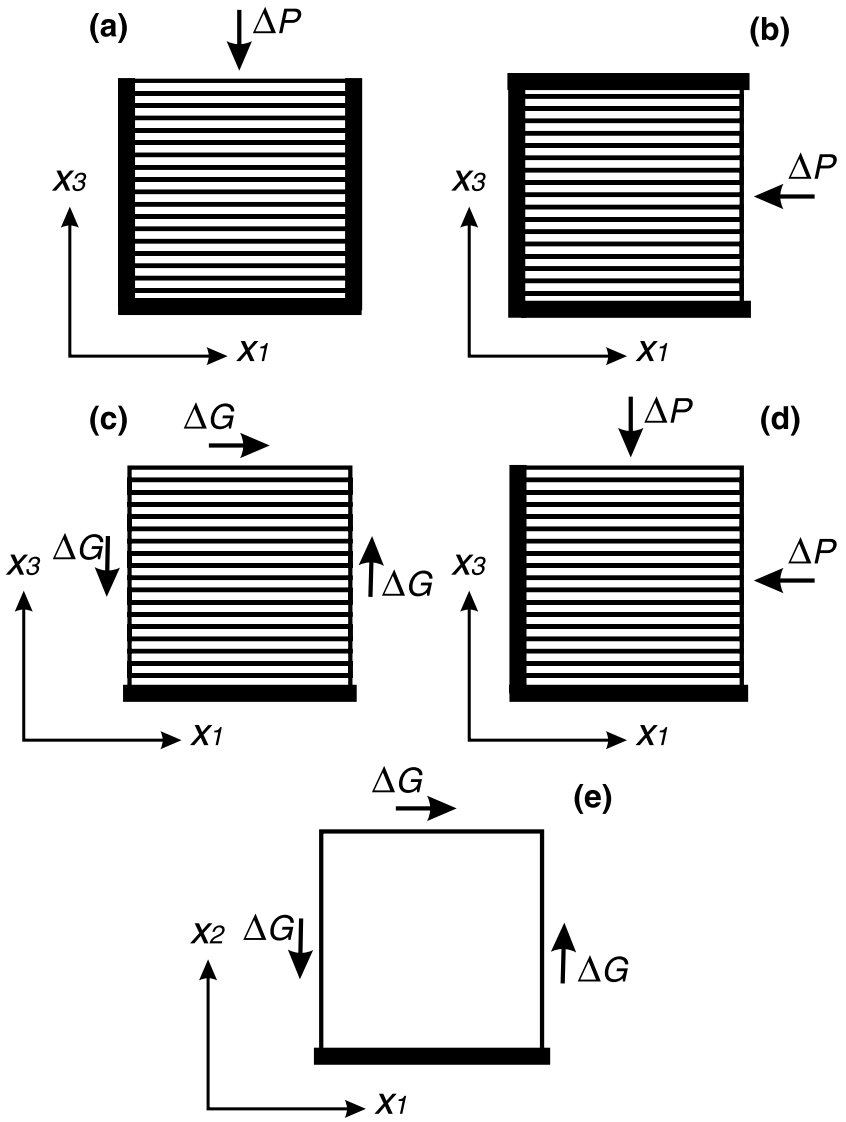

Figure 1. Oscillatory tests performed to obtain p_{33} (a), p_{11} (b), p_{55} (c), p_{13} (d) and p_{66} (e). The orientation of the layers and the directions of the applied stresses are indicated. The thick black lines at the edges indicate rigid boundary conditions (zero displacements).

The change in shape of the rock sample allow us to compute $p_{55}(\omega)$ by using the relation

$$\tan[\theta(\omega)] = \frac{\Delta G}{p_{55}(\omega)}, \tag{33}$$

where $\theta(\omega)$ is the angle between the original positions of the lateral boundaries and the location after applying the shear stresses (Kolsky 1963).

The horizontal displacements $u^s{}_1(x_1, L, \omega)$ at the top boundary Γ^T are used to obtain, for each frequency, an average horizontal displacement $u_1^{s,T}(\omega)$ at the boundary Γ^T. This average value allows us to approximate the change in shape suffered by the sample, given by $\tan[\theta(\omega)] \approx u_1^{s,T}(\omega)/L$, which from eq. (33) yields $p_{55}(\omega)$.

(iv) p_{66}: Since this stiffness is associated with shear waves travelling in the (x_1, x_2)-plane, we take the layered sample, rotate it 90° and apply the shear test as indicated for p_{55}.

(v) p_{13}: The boundary conditions

$$\sigma(u)\nu \cdot \nu = -\Delta P, \quad (x_1, x_3) \in \Gamma^R \cup \Gamma^T, \tag{34}$$

$$\sigma(u)\nu \cdot \chi = 0, \quad (x_1, x_3) \in \Gamma, \tag{35}$$

$$u^s \cdot \nu = 0, \quad (x_1, x_3) \in \Gamma^L \cup \Gamma^B, \tag{36}$$

$$u^f \cdot \nu = 0, \quad (x_1, x_3) \in \Gamma. \tag{37}$$

Thus, in this experiment $\epsilon_{22} = \zeta = 0$, and from eqs (11) and (9) we get

$$\begin{aligned} \tau_{11} &= p_{11}\epsilon_{11} + p_{13}\epsilon_{33}, \\ \tau_{33} &= p_{13}\epsilon_{11} + p_{33}\epsilon_{33}, \end{aligned} \tag{38}$$

where ϵ_{11} and ϵ_{33} are the strain components at the right lateral side and top side of the sample, respectively. Then from eq. (38) and using $\tau_{11} = \tau_{33} = -\Delta P$ [*cf.* eq. (34)], we obtain $p_{13}(\omega)$ as

$$p_{13}(\omega) = \frac{p_{11}\epsilon_{11} - p_{33}\epsilon_{33}}{\epsilon_{11} - \epsilon_{33}}. \tag{39}$$

To estimate the effective complex stiffnesses, we use a FE procedure to approximate the solution of the equations of motion (9) under the boundary conditions described above. We use bilinear functions to approximate the solid displacement vector, while to approximate the fluid displacement a closed subspace of the vector part of the Raviart–Thomas–Nedelec space of zero order was

Table 1. Properties of the Utsira formation.

	Sandstone	Mudstone
Grain bulk modulus, K_s (GPa)	40	20
density, ρ_s (kg m^{-3})	2600	2600
Frame bulk modulus, K_m (GPa)	1.37	7
shear modulus, μ_m (GPa)	0.82	6
porosity, ϕ	0.36	0.2
tortuosity, T	2.8	5
permeability, κ (D)	1.6	0.01
Brine density, ρ_w (kg m^{-3})	1030	1030
viscosity, η_w (Pa s)	0.0012	0.0012
bulk modulus, K_w (GPa)	2.6	2.6
CO_2 density, ρ_g (kg m^{-3})	505	–
viscosity, η_g (Pa s)	0.00015	–
bulk modulus, K_g (MPa)	25	–

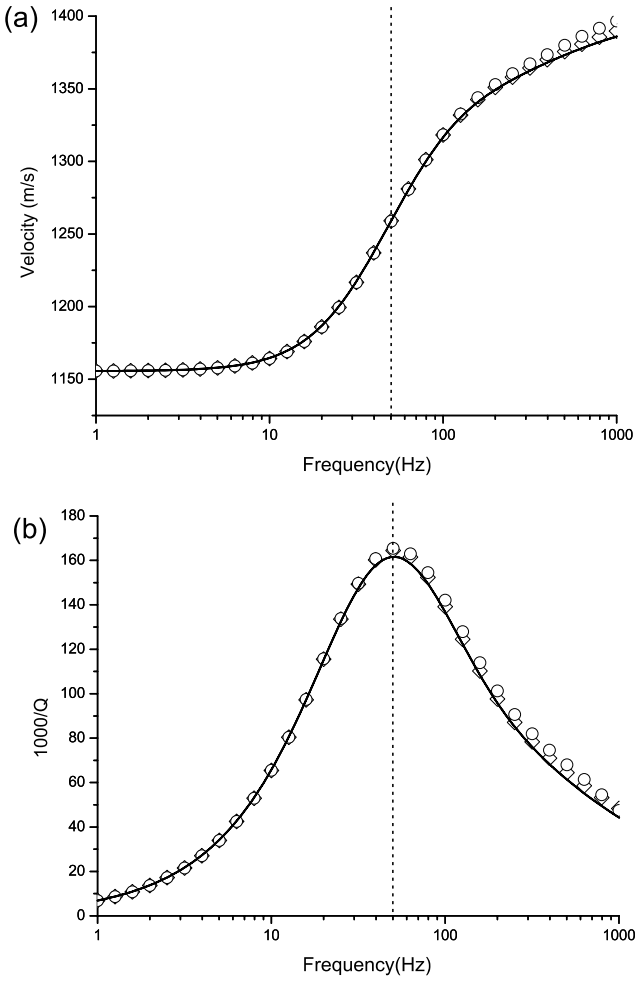

Figure 2. *P*-wave phase velocity (a) and dissipation factor (b) as a function of frequency in the directions parallel (circles and solid line) and perpendicular (diamonds and dashed line) to the layering plane. The symbols correspond to the FE experiments. Here, the analytical solid and dashed curves coincide, since the medium is isotropic. The vertical line indicates the frequency (50 Hz) used for the polar plots. The medium consists of a sequence of gas and brine saturated thin sandstone layers with a gas saturation of 50 per cent ($d_1 = d_2 = 30$ cm).

employed (Raviart & Thomas 1977; Nedelec 1980). The arguments given in Santos *et al.* (2009) to derive a-priori error estimates for the isotropic case can be extended to these FE problems to show that the corresponding errors measured in the energy norm, is of the order of the size of the computational mesh.

4 NUMERICAL EXAMPLES

Let us consider the North-Sea Utsira formation located 800 m below the sea bottom, which contains a highly permeable sandstone, where carbon dioxide (CO_2) has been injected in the Sleipner field (Carcione *et al.* 2006). A typical sample has a porosity of 36 per cent and contains 70 per cent quartz, 10 per cent feldspar, 5 per cent mica, 5 per cent calcite, 5 per cent clay and 5 per cent illite. Using the average of the Hashin–Shtrikman bounds, we obtain the mineral moduli $K_s = 40$ GPa and $\mu_s = 38$ GPa, while the grain density is $\rho_s = 2600$ kg m^{-3}. For $z = 850$ m, a pore pressure $p_f = 10.7$ MPa, confining pressure $p_c = 18$ MPa and temperature $T = 37\,^{\circ}$C, the CO_2 properties are $\rho_g = 505$ kg m^{-3} and $K_g = 0.025$ GPa, and the brine properties (without dissolved gas) are $\rho_w = 1030$ kg m^{-3} and $K_w = 2.6$ GPa. To compute the matrix moduli of the Utsira sand, we use

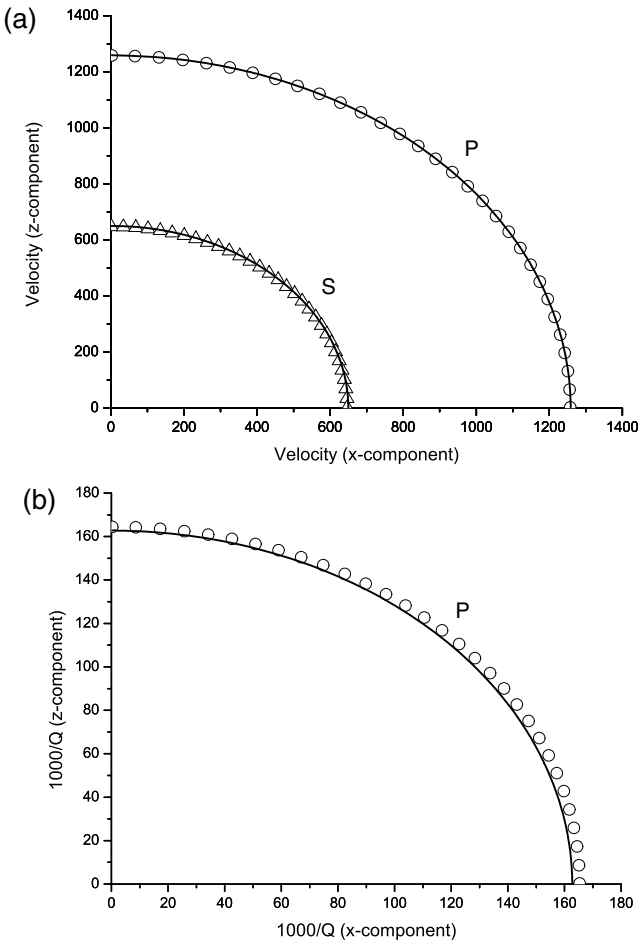

Figure 3. Polar representation of the energy velocity (a) and quality factor (b) corresponding to a frequency of 50 Hz. The medium consist of a sequence of gas and brine saturated thin sandstone layers. The gas saturation is 50 per cent ($d_1 = d_2 = 30$ cm; Fig. 1).

Walton's 'smooth' model and a modified Hashin–Shtrikman lower bound (Carcione *et al.* 2006), because the rock is rather unconsolidated. We obtain $K_m = 1.37$ GPa and $\mu = 0.82$ GPa, giving dry-rock P- and S-wave velocities of 1220 and 704 m s^{-1}, respectively. A summary of the various properties that characterize the sandstone is given in Table 1.

In the plots that follow, symbols denote results from the FE experiments and solid and dashed lines correspond to the analytical solutions. The examples shown here validate the analytical solution of Krzikalla & Müller (2011). First, we consider an alternating sequence of brine and gas saturated sandstone layers of thickness d_1 and d_2, respectively, such that $d = d_1 + d_2 = 0.6$ m. The CO_2 saturation is then given by $S_g = d_2/(d_1 + d_2)$. Fig. 2 shows the P-wave phase velocity (a) and dissipation factor (b) perpendicular to and along the layering plane as a function of frequency and $S_g = 0.5$. The two curves coincide, since the shear modulus is uniform throughout the medium (the effective medium is isotropic and $p_{11} = p_{33}$ and $p_{13} = p_{11} - 2\,p_{55}$). The energy velocity and quality factor versus propagation angle are given in Fig. 3. Since the medium is isotropic, there is no coupling between the P and SV modes and the SV wave is lossless. The P-wave attenuation is rather strong with a quality factor approximately equal to 6 at surface-seismic frequencies (50 Hz).

The second example considers alternating layers of mudstone and sandstone saturated with brine, with thicknesses of 5 and 1 cm, respectively. Within the Utsira aquifer, compacted mudstone layers have been identified (Arts *et al.* 2007), which act as barriers to the upward migration of the CO_2. Table 1 shows the hypothetical poroelastic properties of the mudstone. The upper part of the aquifer (cap rock) can be the case where the proportion of mudstone is substantial. The phase velocity and dissipation factor versus frequency are shown in Fig. 4. The attenuation is higher along the direction perpendicular to the layering plane and the medium is practically lossless along the that plane. Higher attenuation is associated with higher velocity dispersion as can be seen in Fig. 4(a). Fig. 5 shows the energy velocity and dissipation factor versus propagation angle at a frequency of 50 Hz. The three wave modes are indicated in the plots. The velocity anisotropy of the shear modes is substantial, with a noticeable shear-wave splitting. As can be seen, the coupling between the qP and qSV waves generates strong shear attenuation at 45°. This coupling effect is mainly influenced

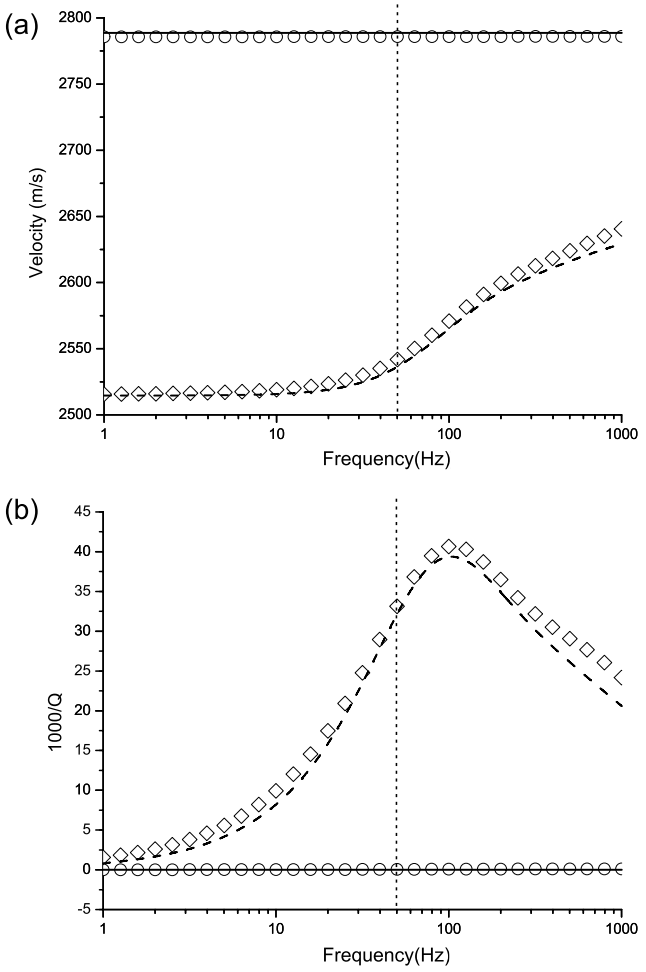

Figure 4. P-wave phase velocity (a) and dissipation factor (b) as a function of frequency in the directions parallel (circles and solid line) and perpendicular (diamonds and dashed line) to the layering plane. The symbols correspond to the FE experiments. The vertical line indicates the frequency (50 Hz) used for the polar plots. The medium consists of a sequence of mudstone and water-saturated sandstone layers of 5 and 1 cm, respectively.

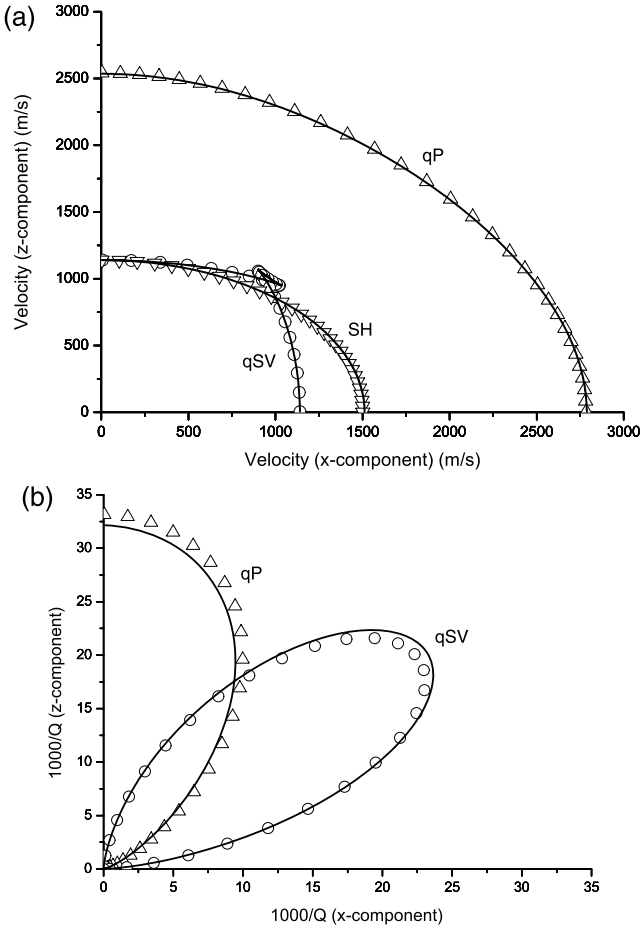

Figure 5. Polar representation of the energy velocity (a) and dissipation factor $[(1000/Q)\,(\sin\theta,\,\cos\theta)]$ (b) corresponding to a frequency of 50 Hz. The medium consists of a sequence of mudstone and water-saturated sandstone layers of 5 and 1 cm, respectively (Fig. 4).

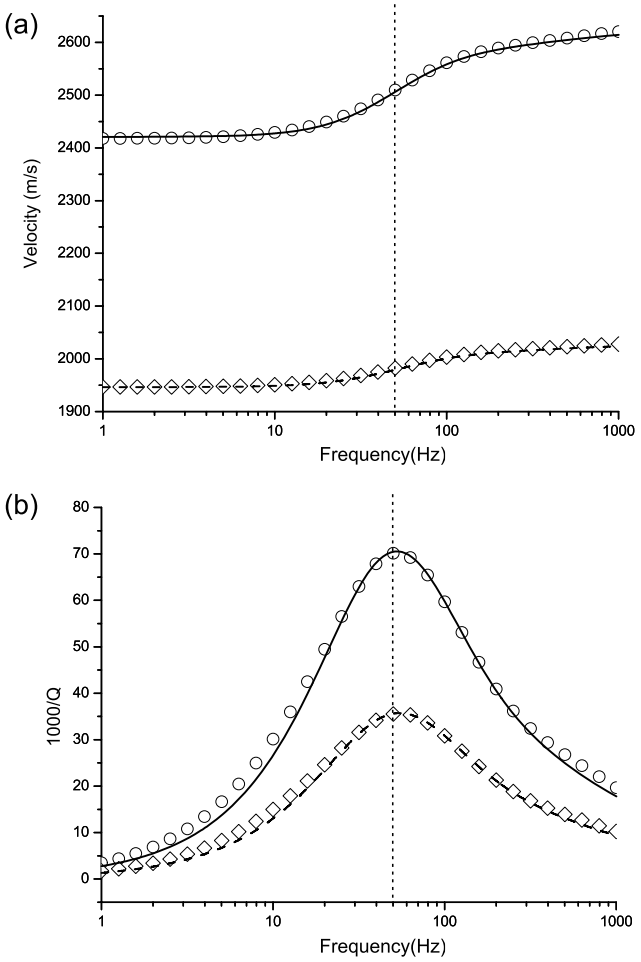

Figure 6. *P*-wave phase velocity (a) and dissipation factor (b) as a function of frequency in the directions parallel (circles and solid line) and perpendicular (diamonds and dashed line) to the layering plane. The symbols correspond to the FE experiments. The vertical dashed line indicates the frequency (50 Hz) used for the polar plots. The medium consist of a sequence of mudstone and CO_2-saturated sandstone layers with thicknesses of 5 and 1 cm, respectively.

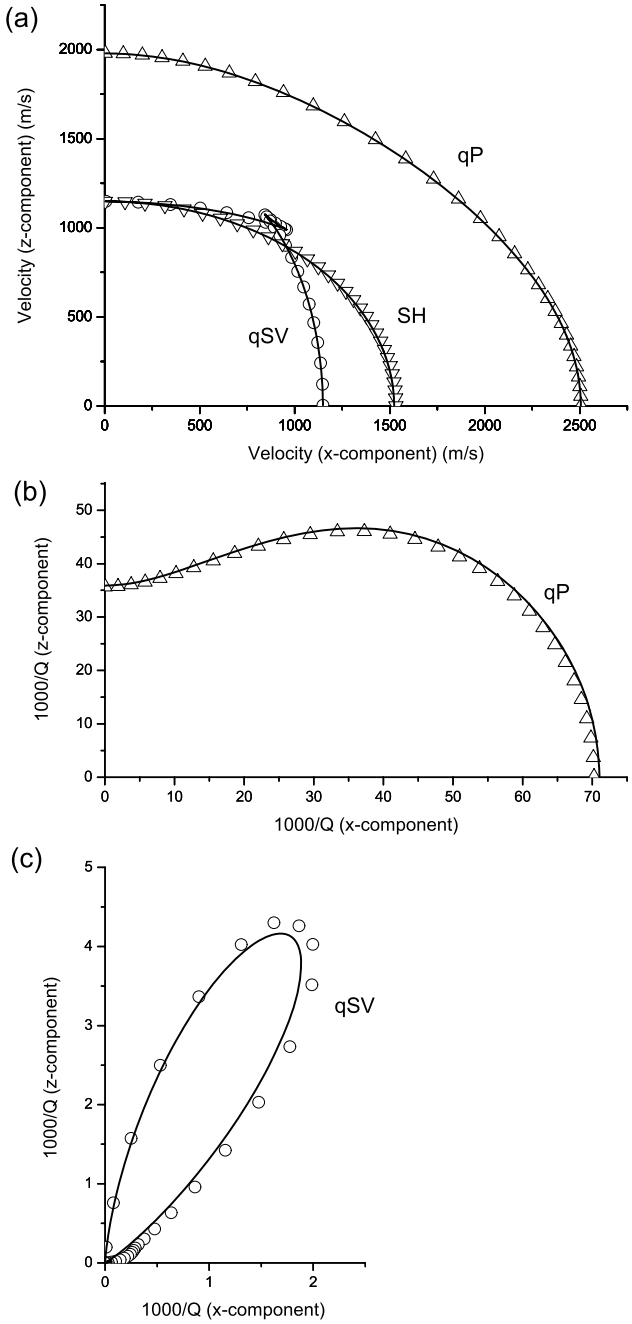

Figure 7. Polar representation of the energy velocity (a) and dissipation factors (b and c) corresponding to a frequency of 50 Hz. The medium consist of a sequence of mudstone and CO_2-saturated sandstone layers with thicknesses of 5 and 1 cm, respectively (Fig. 6).

by the contrast in dry-rock rigidity between the mudstone and the sandstone.

The last example considers alternating layers of mudstone and sandstone saturated with CO_2 of thicknesses 5 and 1 cm, respectively, and a period of 6 cm. In this case, the brine has been replaced by gas and the sequence may represent possible leakages to the cap rock. The phase velocity and dissipation factor versus frequency are shown in Fig. 6. The attenuation is higher along the layering plane, contrary to the prediction of the second example. The energy velocity and dissipation factors as a function of the propagation angle is represented in Fig. 7, where the frequency is 50 Hz. There is a noticeable shear wave splitting as in the previous example. While the *qSV* attenuation curves are qualitative similar to those of the previous case, the *qP* curves show the opposite behaviour with strong attenuation along the layering direction, although in this case the shear attenuation is much weaker than the *qP* attenuation. In this case, maximum shear attenuation occurs at 30°.

5 CONCLUSIONS

We have presented a set of quasi-static harmonic experiments, based on a numerical finite-element method, to determine the equivalent complex and frequency-dependent stiffnesses of a finely layered fluid-saturated porous material, which allow us to compute the wave velocities and quality factors as a function of frequency and propagation angle. These experiments are completely controlled and may be an alternative to or precede the most costly real field or laboratory experiments. The results are compared to analytical

solutions from the Backus/White model, which hold for finely-layered horizontally homogeneous porous media at long wavelengths. The proposed numerical procedure is based on a finite-element solution of the equations of motion in the space-frequency domain to simulate harmonic compressibility and shear tests.

We consider periodic alternating layers saturated with brine and gas, and a sequence of mudstone/sandstone layers with the properties of the North-Sea Utsira aquifer. The medium is isotropic if the solid frame of the layers is uniform, but substantial *P*-wave attenuation is induced by the brine/gas partial saturation. On the other hand, when the properties of the frame varies, such in the mudstone/sandstone sequence, velocity and attenuation anisotropy can be observed in the *qP* and *qSV* wave modes. In this case, the attenuation is stronger along the direction perpendicular to layering if the sandstone is saturated with brine, while the opposite behaviour occurs if the fluid is gas, that is, there is more attenuation along the layering plane. The shear wave has no loss along the directions parallel and perpendicular to the layering plane, and has maximum attenuation around 45°, with magnitudes comparable to those of the *qP* wave. The coupling is mainly determined by contrast in the dry-rock moduli. On the other hand, the SH wave is lossless. The agreement between the numerical and analytical results for the examples presented here is very good, although further tests are necessary to verify the 1-D character of the fluid flow.

The numerical solver proposed in this work can be applied to more complex geological situations (lower symmetries, stochastic heterogeneities, fractures, etc.) and implemented in the processing and interpretation of real seismic data for characterization purposes.

ACKNOWLEDGMENTS

This work has been partially funded by the European Union under the framework of the CO2CARE project. We thank Fabian Krzikalla and Tobias Müller for providing a preprint of their manuscript.

REFERENCES

Arts, R.J., Chadwick, R.A., Eiken, O., Trani, M. & Dortland, S., 2007. Synthetic versus real time-lapse seismic data at the Sleipner CO_2 injection site, *SEG Expand. Abstr.*, **26**, 2974, doi:10.1190/1.2793089.

Backus, G.E., 1962. Long-wave elastic anisotropy produced by horizontal layering, *J. geophys. Res.*, **67**, 4427–4440.

Biot, M.A., 1962. Mechanics of deformation and acoustic propagation in porous media, *J. appl. Phys.*, **33**, 1482–1498.

Bruggeman, D.A.G., 1937. Berechnungen der verschiedener physikalischen Konstanten von heterogenen Substanzen. III: die elastischen Konstanten der quasi-isotropen Mischkörper aus isotropen Substanzen, *Annalen der Physik*, **29**, 160–178.

Carcione, J.M., 1992. Anisotropic Q and velocity dispersion of finely layered media, *Geophys. Prospect.*, **40**, 761–783.

Carcione, J.M., 2007. Wave fields in real media: wave propagation in anisotropic, anelastic, porous and electromagnetic media, in *Handbook of Geophysical Exploration*, 2nd edn, Vol. 38, 515pp., eds Helbig, K. & Treitel, S., Elsevier, Oxford.

Carcione, J.M. & Picotti, S., 2006. P-wave seismic attenuation by slow-wave diffusion, Effects of inhomogeneous rock properties, *Geophysics*, **71**, O1–O8.

Carcione, J.M., Picotti, S., Gei, D. & Rossi, G., 2006. Physics and seismic modeling for monitoring CO_2 storage, *Pure appl. Geophys.*, **163**, 175–207.

Carcione, J.M., Morency, C. & Santos, J.E., 2010. Computational poroelasticity—a review, *Geophysics*, **75**, A229–A243.

Gelinsky, S. & Shapiro, S.A., 1997. Poroelastic backus-averaging for anisotropic, layered fluid and gas saturated sediments, *Geophysics*, **62**, 1867–1878.

Kolsky, H., 1963. *Stress Waves in Solids*, Dover publications, New York.

Krzikalla, F. & Müller, T., 2011. Anisotropic P-SV-wave dispersion and attenuation due to inter-layer flow in thinly layered porous rocks, *Geophysics*, **76**, WA135, doi:10.1190/1.3555077.

Müller, T., Gurevich, B. & Lebedev, M., 2010. Seismic wave attenuation and dispersion resulting from wave-induced flow in porous rocks—a review, *Geophysics*, **75**, A147–A164.

Nedelec, J.C., 1980. Mixed finite elements in R^3, *Numer. Math.*, **35**, 315–341.

Picotti, S., Carcione, J.M., Santos, J.E. & Gei, D., 2010. Q-anisotropy in finely-layered media, *Geophys. Res. Lett.*, **37**, L06302, doi:10.1029/2009GL042046.

Postma, G.W., 1955. Wave propagation in a stratified medium, *Geophysics*, **20**, 780–806.

Pride, S.R., Berryman, J.G. & Harris, J.M., 2004. Seismic attenuation due to wave-induced flow, *J. geophys. Res.*, **109**, B01201, doi:10.1029/2003JB002639.

Raviart, P.A. & Thomas, J.M., 1977. Mixed finite element method for 2nd order elliptic problems, *Mathematical Aspects of the Finite Element Methods*, Lecture Notes of Mathematics, Vol. 606, pp. 292–315, eds Galligani, I. & Magenes, E., Springer-Verlag, New York, NY.

Riznichenko, Y.V., 1949. Seismic quasi-anisotropy, *Bull. Acad. Sci. USSR, Geograph. Geophys. Serv.*, **13**, 518–544.

Santos, J.E., Rubino, J.G. & Ravazzoli, C.L., 2009. A numerical upscaling procedure to estimate effective plane wave and shear moduli in heterogeneous fluid-saturated poroelastic media, *Comput. Methods Appl. Mech. Eng.*, **198**, 2067–2077.

Santos, J.E., Carcione, J.M. & Picotti, S., 2011. Viscoelastic-stiffness tensor of anisotropic media from oscillatory numerical experiments, *Comput. Methods Appl. Mech. Eng.*, **200**, 896–904.

Wenzlau, F., Altmann, J.B., Mller, T.M., 2010. Anisotropic dispersion and attenuation due to wave-induced flow: quasi-static finite-element modeling in poroelastic solids, *J. geophys. Res.*, **115**, B07204, doi:10.1029/2009JB006644.

White, J.E., Mikhaylova, N.G. & Lyakhovitskiy, F.M., 1975. Low-frequency seismic waves in fluid saturated layered rocks, *Phys. Solid Earth*, **11**, 654–659.

APPENDIX A: MESOSCOPIC-FLOW ATTENUATION THEORY FOR ANISOTROPIC POROELASTIC MEDIA

White's mesoscopic attenuation theory of interlayer flow (White *et al.* 1975; Carcione & Picotti 2006) describes the equivalent viscoelastic medium of a stack of two thin alternating porous layers of thickness d_1 and d_2, such that the period of the stratification is $d = d_1 + d_2$. The theory gives the complex and frequency dependent stiffness p_{33}. White model has been generalized by Krzikalla & Müller (2011) to anisotropic media, that is, they have obtained the five stiffnesses of the equivalent transversely isotropic medium, denoted by p_{IJ}. The stress-strain relations is given by eqs (10)–(15) and

$$p_{IJ}(\omega) = c_{IJ} + \left(\frac{c_{IJ} - c^r_{IJ}}{c_{33} - c^r_{33}}\right)[p_{33}(\omega) - c_{33}], \tag{A1}$$

where c^r_{IJ} and c_{IJ} are the relaxed and unrelaxed stiffnesses.

According to Gelinsky & Shapiro (1997) [their eq. (14)], the quasi-static or relaxed effective constants of a stack of poroelastic

layers are

$$c^r_{66} = B^*_1 = \langle \mu \rangle,$$

$$c^r_{11} - 2c^r_{66} = c^r_{12} = B^*_2 = 2\left\langle \frac{\lambda_m \mu}{E_m} \right\rangle + \left\langle \frac{\lambda_m}{E_m} \right\rangle^2 \left\langle \frac{1}{E_m} \right\rangle^{-1} + \frac{B^{*2}_6}{B^*_8},$$

$$c^r_{13} = B^*_3 = \left\langle \frac{\lambda_m}{E_m} \right\rangle \left\langle \frac{1}{E_m} \right\rangle^{-1} + \frac{B^*_6 B^*_7}{B^*_8},$$

$$c^r_{33} = B^*_4 = \left\langle \frac{1}{E_m} \right\rangle^{-1} + \frac{B^{*2}_7}{B^*_8}$$

$$= \left[\left\langle \frac{1}{E_m} \right\rangle - \left\langle \frac{\alpha}{E_m} \right\rangle^2 \left\langle \frac{E_G}{M E_m} \right\rangle^{-1} \right]^{-1},$$

$$c^r_{55} = B^*_5 = \langle \mu^{-1} \rangle^{-1},$$

$$B^*_6 = -B^*_8 \left(2\left\langle \frac{\alpha \mu}{E_m} \right\rangle + \left\langle \frac{\alpha}{E_m} \right\rangle \left\langle \frac{\lambda_m}{E_m} \right\rangle \left\langle \frac{1}{E_m} \right\rangle^{-1} \right),$$

$$B^*_7 = -B^*_8 \left\langle \frac{\alpha}{E_m} \right\rangle \left\langle \frac{1}{E_m} \right\rangle^{-1},$$

$$B^*_8 = \left[\left\langle \frac{1}{M} \right\rangle + \left\langle \frac{\alpha^2}{E_m} \right\rangle - \left\langle \frac{\alpha}{E_m} \right\rangle^2 \left\langle \frac{1}{E_m} \right\rangle^{-1} \right]^{-1}, \quad \text{(A2)}$$

where

$$\lambda_m = K_m - \frac{2}{3}\mu \quad \text{and} \quad E_m = K_m + \frac{4}{3}\mu \quad \text{(A3)}$$

and we have also reported the notation of that paper for clarity. In the case of no interlayer flow, that is, the unrelaxed regime, the stiffnesses are

$$c_{66} = c^r_{66},$$

$$c_{11} - 2c_{66} = c_{12} = 2\left\langle \frac{(E_G - 2\mu)\mu}{E_G} \right\rangle + \left\langle \frac{E_G - 2\mu}{E_G} \right\rangle^2 \left\langle \frac{1}{E_G} \right\rangle^{-1},$$

$$c_{13} = \left\langle \frac{E_G - 2\mu}{E_G} \right\rangle \left\langle \frac{1}{E_G} \right\rangle^{-1},$$

$$c_{33} = \left\langle \frac{1}{E_G} \right\rangle^{-1},$$

$$c_{55} = c^r_{55} \quad \text{(A4)}$$

[Gelinsky & Shapiro (1997), eq. (15)], where

$$E_G = E_m + \alpha^2 M \quad \text{(A5)}$$

is Gassmann's *P*-wave modulus. Gassmann's bulk modulus is K_G as given in eq. (4).

Finally, the *P*-wave modulus p_{33} is (White *et al.* 1975; Carcione & Picotti 2006) [see also Carcione (2007), eq. (7.400)]

$$p_{33} = \left[\frac{1}{c_{33}} + \frac{2(r_2 - r_1)^2}{\mathrm{i}\omega(d_1 + d_2)(I_1 + I_2)} \right]^{-1}. \quad \text{(A6)}$$

where

$$r = \frac{\alpha M}{E_G} \quad \text{(A7)}$$

and

$$I = \frac{\eta}{\kappa a} \coth\left(\frac{ad}{2} \right), \quad a = \sqrt{\frac{\mathrm{i}\omega\eta E_G}{\kappa M E_m}}, \quad \text{(A8)}$$

for each single layer.

The assumptions in Krzikalla & Müller (2011) theory are:

(i) The stiffnesses matrix is symmetric (see Carcione (2007), eq. (2.24) and related discussion);

(ii) The fluid-flow direction (perpendicular to layering) is independent of the loading direction and the relaxation behaviour is described by a single relaxation function or stiffness, that is, $p_{33}(\omega)$. This means that that the theory is valid for plane layers and that a single relaxation function cannot be used in the case of 2-D or 3-D heterogeneities;

(iii) The stiffness p_{33} used here corresponds to a periodic medium (period = $d_1 + d_2$) composed of two materials.

The fact that the relaxed and unrelaxed shear moduli coincide [see eq. (A4)] implies that there is no shear loss along the directions perpendicular and parallel to layering. The *qSV* wave is dispersive due to its coupling with the *qP* wave, but the horizontally polarized SH wave is not dispersive, since $c_{55} = c^r_{55}$ and $c_{66} = c^r_{66}$ imply $p_{55} = c_{55}$ and $p_{66} = c_{66}$, according to eq. (A1). Moreover, an alternating sequence of thin layers saturated with different fluids but having the same shear modulus does not generate anisotropy. If there are no changes in the shear moduli, the long-wavelength equivalent Backus medium is isotropic.

Following Gelinsky & Shapiro (1997), the average medium has the density

$$\bar{\rho} = \langle \rho \rangle, \quad \text{(A9)}$$

where ρ is given in eq. (5).

The approximate transition frequency separating the relaxed and unrelaxed states (i.e. the approximate location of the relaxation peak) is (Carcione 2007)

$$f_0 = \frac{8\kappa M E_m}{\pi \eta d^2 E_G}, \quad \text{(A10)}$$

where M, E_G, η and d refer to each single layer. At this reference frequency, the Biot slow-wave attenuation length equals the mean layer thickness or characteristic length of the inhomogeneities (see next paragraph). Eq. (A10) indicates that the mesoscopic loss mechanism moves towards the low frequencies with increasing viscosity and decreasing permeability, that is, the opposite behaviour of the Biot relaxation mechanism.

The mesoscopic loss mechanism is due to the presence of the Biot slow wave and the diffusivity constant is $D = \kappa M E_m/(\eta E_G)$ (Carcione 2007). The critical fluid-diffusion relaxation length is $L = \sqrt{D/\omega}$. The fluid pressures will be equilibrated if L is comparable to the period of the stratification. For smaller diffusion lengths (e.g. higher frequencies) the pressures will not be equilibrated, causing attenuation and velocity dispersion. Note that the reference frequency (A10) is obtained for a diffusion length $L = d_1/4$.

APPENDIX B: WAVE VELOCITIES AND QUALITY FACTORS

We consider homogeneous viscoelastic waves (Carcione 2007). The complex velocities are the key quantity to obtain the wave velocities and quality factor of the equivalent anisotropic medium. They are

given by (Carcione 2007)

$$
\begin{aligned}
v_{\rm qP} &= (2\bar{\rho})^{-1/2}\sqrt{p_{11}l_1^2 + p_{33}l_3^2 + p_{55} + A}\\
v_{\rm qSV} &= (2\bar{\rho})^{-1/2}\sqrt{p_{11}l_1^2 + p_{33}l_3^2 + p_{55} - A}\\
v_{\rm SH} &= \bar{\rho}^{-1/2}\sqrt{p_{66}l_1^2 + p_{55}l_3^2}\\
A &= \sqrt{\left[(p_{11} - p_{55})l_1^2 + (p_{55} - p_{33})l_3^2\right]^2 + 4[(p_{13} + p_{55})l_1l_3]^2},
\end{aligned}
\tag{B1}
$$

where $l_1 = \sin\theta$ and $l_3 = \cos\theta$ are the directions cosines, θ is the propagation angle between the wavenumber vector and the symmetry axis, and the three velocities correspond to the *qP*, *qS* and *SH* waves, respectively. The phase velocity is given by

$$
v_p = \left[{\rm Re}\left(\frac{1}{v}\right)\right]^{-1}, \tag{B2}
$$

where v represents either $v_{\rm qP}$, $v_{\rm qSV}$ or $v_{\rm SH}$. The energy-velocity vector of the *qP* and *qSV* waves is given by

$$
\frac{v_e}{v_p} = (l_1 + l_3\cot\psi)^{-1}\hat{\mathbf{e}}_1 + (l_1\tan\psi + l_3)^{-1}\hat{\mathbf{e}}_3. \tag{B3}
$$

(Carcione 2007, eq. 6.158), where

$$
\tan\psi = \frac{{\rm Re}(\beta^* X + \xi^* W)}{{\rm Re}(\beta^* W + \xi^* Z)}, \tag{B4}
$$

defines the angle between the energy-velocity vector and the z-axis,

$$
\begin{aligned}
\beta &= \sqrt{A \pm B},\\
\xi &= \pm{\rm pv}\sqrt{A \mp B},\\
B &= p_{11}l_1^2 - p_{33}l_3^2 + p_{55}\cos 2\theta,
\end{aligned}
\tag{B5}
$$

where the upper and lower signs correspond to the *qP* and qS waves, respectively. Moreover,

$$
\begin{aligned}
W &= p_{55}(\xi l_1 + \beta l_3),\\
X &= \beta p_{11}l_1 + \xi p_{13}l_3,\\
Z &= \beta p_{13}l_1 + \xi p_{33}l_3
\end{aligned}
\tag{B6}
$$

(Carcione 2007, eqs. 6.121–6.123), where 'pv' denotes the principal value, which has to chosen according to established criteria.

On the other hand, the energy velocity of the SH wave is

$$
\mathbf{v}_e = \frac{1}{\bar{\rho}v_p}(l_1c_{66}\hat{\mathbf{e}}_1 + l_3c_{55}\hat{\mathbf{e}}_3) \tag{B7}
$$

and

$$
\tan\psi = \left(\frac{c_{66}}{c_{55}}\right)\tan\theta \tag{B8}
$$

(Carcione 2007, eq. 1.148), since p_{55} and p_{66} are real quantities.

In general, the phase velocity is related to the energy velocity by

$$
v_p = v_e\cos(\psi - \theta), \tag{B9}
$$

where $v_e = |\mathbf{v}_e|$. The quality factor is given by

$$
Q = \frac{{\rm Re}(v^2)}{{\rm Im}(v^2)}. \tag{B10}
$$

The values of the *qP* quality factor along the layering plane and symmetry axis are

$$
Q_P(\theta = \pi/2) = \frac{{\rm Re}(p_{11})}{{\rm Im}(p_{11})} \quad \text{and} \quad Q_P(\theta = 0) = \frac{{\rm Re}(p_{33})}{{\rm Im}(p_{33})}, \tag{B11}
$$

respectively, while those of the shear waves are infinite along those directions.